Article

Control Strategy for Disc Coreless Permanent Magnet Synchronous Motor with LC Filter

Hong Tian and Min Kang *

School of Automation and Electrical Engineering, Zhejiang University of Science and Technology, Hangzhou 310023, China; 222107855026@zust.edu.cn
* Correspondence: kangmin@zust.edu.cn

Abstract: The disc coreless permanent magnet synchronous motor has the advantages of a short axial size, high power density, and small volume. Due to the coreless structure, its inductance is very small, which results in a serious current ripple and an unacceptable torque ripple if driven from a conventional inverter. This can be solved by installing an LC filter between the inverter and the motor. However, an undesirable resonance phenomenon is induced by the LC filter. In this paper, a new capacitive current feedback active damping (CCFAD) strategy is proposed. Instead of current sensors in the capacitor branch, a state observer is introduced to estimate the capacitance current. The observer is designed with double sliding mode surfaces, which reduces the order of the system. Compared to conventional capacitive current feedback, no additional current sensors are required, reducing the system cost. Besides the resonant harmonics, the phase current contains obvious fifth and seventh harmonics due to the special plane structure of the rotor. The proportional-integral-resonance (PIR) controller, instead of the traditional PI controller, is designed to suppress lower order harmonics. The experiment results show that current ripples due to resonance and rotor structure are suppressed significantly.

Keywords: disc coreless permanent magnet synchronous motor; LC filter; capacitor current feedback active damping (CCFAD); state observer; proportional-integral-resonance (PIR)

1. Introduction

Disc coreless permanent magnet synchronous motors have attracted much attention in academia and industry due to their unique disc structure and high efficiency [1]. This motor gradually shows great potential in its high torque density and small volume, especially in the key fields such as transportation, and its application value is more prominent [2].

Due to the elimination of the iron core from the stator, the inductance value of stator winding is extremely small. Therefore, when the motor is fed by the conventional controller, the motor phase current ripple is very large, which will cause a large electromagnetic torque ripple. Approaches for current ripple attenuation in small-inductance motors involve increasing switching frequencies, employing multilevel drive, and utilizing external filters [3]. The higher switching frequency can be achieved by SiC devices [4]. Nonetheless, the production process of silicon carbide devices is relatively complex and the cost is significantly high, so the choice of switching frequency requires a trade-off between ripple reduction and cost. Another feasible solution is to use a modular multilevel inverter to suppress the stator current ripple [5]. There is no doubt that multilevel topology means more switching devices, which greatly increases the volume and price of the driver, and is not suitable for most applications considering size and economy. Among the available methods, an LC filter can be also adopted to suppress the current ripple [6]. The LC filter and motor inductance are combined to form an LCL filter, which has a stronger high-frequency ripple attenuation ability [7–10]. Figure 1 shows the coreless motor drive system with an LC filter.
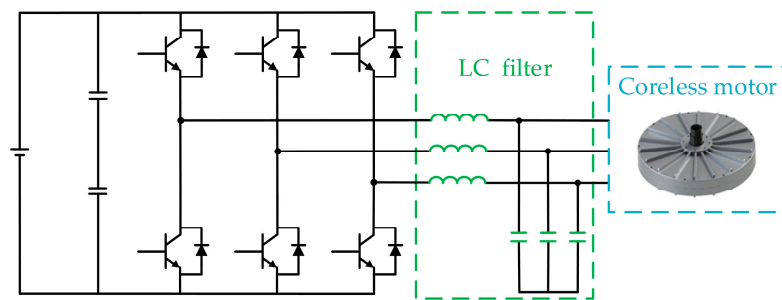
Figure 1. Drive system of the coreless motor with an LC filter.

The LCL filter is a high-order system. When there is no damping, the system will produce a serious resonance phenomenon, which puts forward higher requirements for the stability and performance of the system [11]. The two main methods to reduce the resonance peaks of LCL-type filters are passive damping and active damping. Passive damping is a common method to enhance the stability of LCL filter systems. For instance, the resonance problem can be suppressed by using additional resistance in the capacitor branch. Although the implementation is simple and fast, it will inevitably increase the loss and reduce the suppression of harmonic components by the filter [12,13].

Active damping solutions are popularly investigated to suppress the resonance phenomenon of the LCL filter. The advantage of this method is that no additional passive components are required. In [14], an active damping control strategy based on capacitor current feedback is proposed, but extra current sensors are required. Similarly, an active damping method based on capacitive voltage feedback is proposed, which is equivalent to connecting a virtual damping resistor in series with the capacitive branch [15]. A feedforward approach suppresses resonance, where the feedforward term is subtracted from the stator current reference. Nonetheless, the capacitor currents are estimated from the reference voltages of the inverter; therefore, additional voltage sensors are required [16]. Reducing the control delay time can improve the stability of the LCL filter system, but this method requires a high sampling frequency, which is difficult to achieve in practical applications [17]. The design method of the active damping controller in the model predictive current controller has been studied, but there are many parameters to be designed [18,19].

In the above method, capacitive current damping is an effective and feasible solution. However, in the motor drive, the current sensor is usually welded on the inverter board. The traditional method to obtain capacitive current is to install current sensors in the capacitor branch of the filter or the motor side, but these methods are not conducive to the modular production of the driver and they increase the cost. To solve this problem, a sliding mode current observer is designed in this paper based on the mathematical model of the system. Firstly, the observer is used to estimate the motor current, and then the capacitor current is obtained by subtracting the motor current from the inverter side current.

In the coreless motor drive system with an LC filter, in addition to the resonant harmonics induced by the filter, there are also fifth and seventh harmonic currents caused by the rotor structure design, and inverter nonlinear factors. These lower order harmonics can also cause torque ripple and an increased power loss [20,21]. The PIR control is an effective harmonic control strategy, and is free from complicated coordinate systems [22–24]. Nonetheless, the performance of the PIR controller has only been verified in conventional controllers; none of the research analyzed has been verified in motor drives with LC filters. The design of PIR controllers needs to simultaneously consider the crossover frequency, the amplitude gain, and the phase margin. Moreover, the high-order LCL filter has strict requirements on the accuracy and stability of the PIR controller; especially when considering the active damping, the reasonable parameter optimization design is required. Therefore, it is necessary to make a detailed theoretical analysis.

In summary, the phase currents of the coreless motor contain amounts of harmonic signals that need to be suppressed. To solve these harmonics, a control strategy combining

proportional-integral-resonance and capacitor current feedback active damping is proposed, and the PIR+CCFAD controller composed of proportional, integral, resonant, and capacitor current feedback is designed. The contribution of this article can be concluded as follows:

(1) For resonant harmonics, in order to only measure the inverter side currents, a sliding mode observer is introduced to estimate the capacitance current. The observer is designed with double sliding mode surfaces, which reduces the order of the system.

(2) For fifth and seventh harmonics, in order to free them from complicated coordinate systems, the PIR+CCFAD controller is designed. The transfer function of the PIR controller in the motor drive system with an LC filter is derived, and the optimal design of the control parameters is completed by the bode diagram.

The rest of this paper is organized as follows. The mathematical model of the permanent magnet motor system with an LC filter is proposed in Section 2. Then, in Section 3, the resonance phenomenon of the filter and the proposed observer damping algorithm are analyzed in detail. In Section 4, the transfer function derivation and stability analysis of the PIR+CCFAD controller are completed. In Section 5, the experimental results verify the effectiveness of the proposed control strategy. Finally, a conclusion is drawn in Section 6.

2. Mathematical Model of the Permanent Magnet Synchronous Motor with an LC Filter

The LC filter is installed between the inverter and motor to suppress high-frequency ripples. The mathematical model of the motor with an LC filter in a stationary coordinate system is given as [25]

$$\begin{cases} u_{s\alpha} = R_s\, i_{s\alpha} + L_s \frac{di_{s\alpha}}{dt} + e_{s\alpha} \\ u_{s\beta} = R_s i_{s\beta} + L_s \frac{di_{s\beta}}{dt} + e_{s\beta} \end{cases} \tag{1}$$

$$\begin{cases} L_f \frac{di_{i\alpha}}{dt} = u_{i\alpha} - u_{s\alpha} \\ L_f \frac{di_{i\beta}}{dt} = u_{i\beta} - u_{s\beta} \end{cases} \tag{2}$$

$$\begin{cases} C_f \frac{du_{s\alpha}}{dt} = i_{i\alpha} - i_{s\alpha} \\ C_f \frac{du_{s\beta}}{dt} = i_{i\beta} - i_{s\beta} \end{cases} \tag{3}$$

$$\begin{cases} i_{c\alpha} = i_{i\alpha} - i_{s\alpha} \\ i_{c\beta} = i_{i\beta} - i_{s\beta} \end{cases} \tag{4}$$

where $u_{s\alpha}$ and $u_{s\beta}$ are the motor voltages, $i_{s\alpha}$ and $i_{s\beta}$ are the motor currents, R_s is the motor stator resistance, L_s is the motor stator inductance, $e_{s\alpha}$ and $e_{s\beta}$ are the motor back EMF, L_f is the inductance of the LC filter, C_f is the filter capacitance, $u_{i\alpha}$ and $u_{i\beta}$ are the LC filter input voltages, $i_{i\alpha}$ and $i_{i\beta}$ are the LC filter input currents, and $i_{c\alpha}$ and $i_{c\beta}$ are the filter capacitance currents.

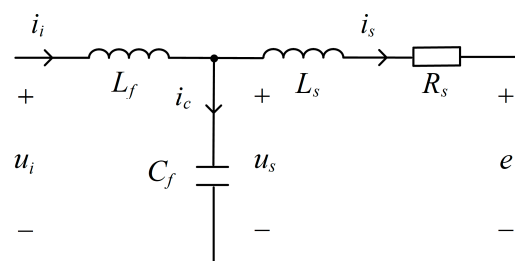Figure 2 shows the LCL structure consisting of an LC filter and a motor inductor.

Figure 2. Diagram of the base structure of the LCL filter.

The voltage drop caused by the stator resistance and the cross-coupling effect are regarded as disturbances and can be ignored, and the simplified system transfer function can be expressed as

$$G(s) = \frac{i_s(s)}{u_i(s)} = \frac{1}{L_f\, L_s C_f\, s^3 + (L_f + L_s)s} \tag{5}$$

Due to the complexity of the cut-off frequency calculation, the resonance frequency is usually approximated as the filter cut-off frequency when the calculation accuracy is not required, and the resonance frequency is expressed as

$$f_r = \frac{1}{2\pi} \sqrt{\frac{L_f + L_s}{L_f \ L_s C_f}} \tag{6}$$

3. Capacitor Current Feedback Active Damping (CCFAD) Resonant Suppression

3.1. Resonance Analysis

The traditional current loop of the permanent magnet synchronous motor in a synchronous rotating coordinate system is shown in Figure 3, i_{sq}^* is the reference current. Taking the q-axis as an example, the open-loop transfer function of the current loop is

$$G_{\text{PI}}(s) = \frac{K_p \ s + K_i}{L_f \ L_s C_f \ s^4 + (L_f \ + L_s)s^2} e^{-T_d S} \tag{7}$$

where K_p is the proportional gain; K_i is the integral gain; and T_d is the system delay time.
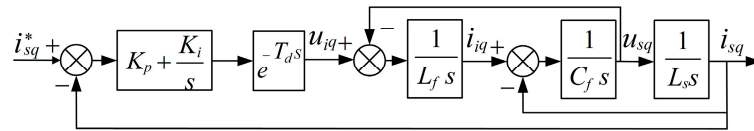

Figure 3. Block diagram of the PI controller.

Figure 4 shows the bode diagrams of the open-loop transfer function with the PI controller. The parameters are set to K_p = 8, K_i = 100, L_f = 0.4 mH, C_f = 10 μF, L_s = 0.1 mH, and T_d = 0.0000625 s. It can be seen that the LCL filter has little effect at a low frequency, but has a strong ability to suppress ripples in a high-frequency range. However, the LCL filter has a high resonance peak at the resonance frequency, which means that the system is only damped a little at the resonance frequency. If this resonant peak is not suppressed, a small voltage may produce a very large current, which will cause the drive system to fail to operate normally. Figure 5 shows the bode diagrams of the closed-loop transfer function with the PI controller. When the coreless motor is operating at 1600 rpm, the sixth harmonic current frequency is 1920 Hz. The corresponding phase margin is −394°, so the PI controller does not track the lower harmonic signals well.
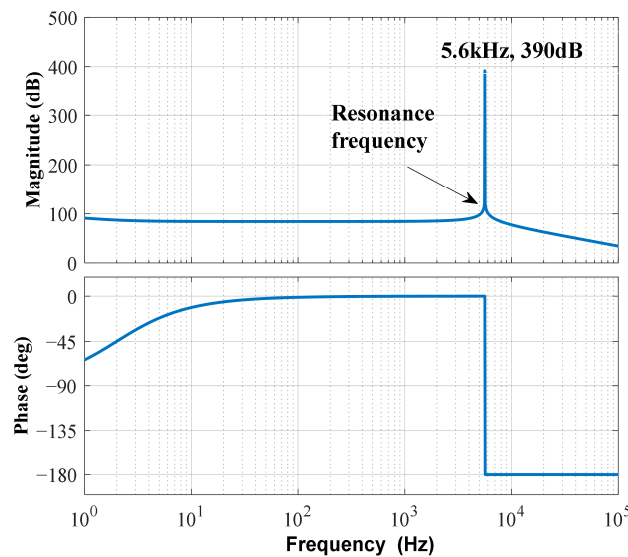

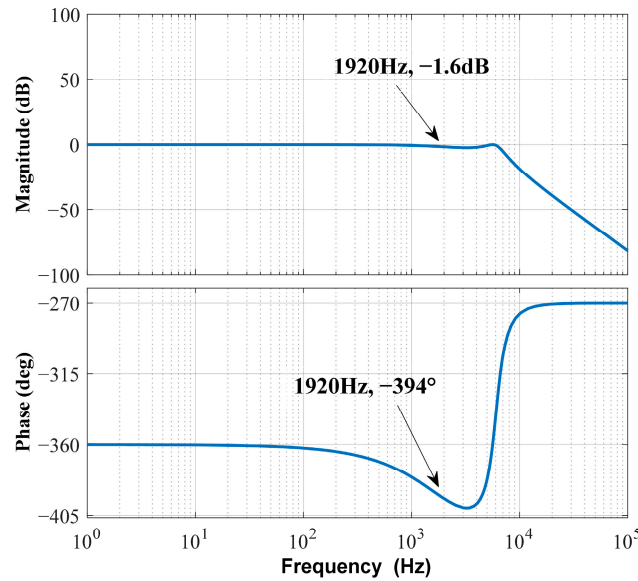**Figure 4.** Bode diagram of the open-loop transfer function with the PI controller.

Figure 5. Bode diagram of the closed-loop transfer function with the PI controller.

3.2. Active Damping

According to the above analysis, the control system with the LC sine wave filter cannot operate stably when using traditional current loop control. In this paper, the proportional feedback active damping strategy of capacitive current is adopted. The control block diagram is shown in Figure 6.
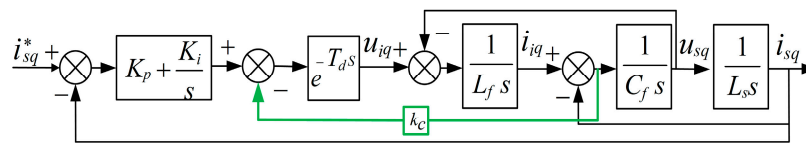

Figure 6. Block diagram of the PI+CCFAD controller.

Where k_c is the active damping coefficient and the open-loop transfer function is

$$G_{\text{PI\_C}}(s) = \frac{K_p s + K_i}{L_f L_s C_f s^4 + k_c L_s C_f e^{-T_d S} s^3 + (L_f + L_s) s^2} e^{-T_d S} \tag{8}$$

Figure 7 shows the bode diagrams of the open-loop transfer function with the PI+CCFAD controller. The parameters are set to $K_p = 8$, $K_i = 100$, $L_f = 0.4$ mH, $C_f = 10$ µF, $L_s = 0.1$ mH, $T_d = 0.0000625$ s, and $k_c = 20$. It can be seen that the resonant peak is effectively suppressed. With the increase in feedback coefficient k_c, the resonant peak decreases gradually. Therefore, the stable operation of the system is ensured by selecting the appropriate active damping coefficient. Figure 8 shows the bode diagrams of the closed-loop transfer function with the PI+CCFAD controller. The corresponding phase margin is $-39°$ in the sixth harmonic current frequency, so the PI+CCFAD controller does not track the lower harmonic signals well.

3.3. State Observer Active Damping

The most direct way to obtain the capacitive current is to install a current sensor in the capacitive branch of the LC filter, but this method is not conducive to the modular production of filters. To solve this problem, the LC filter and motor can be regarded as a whole structure, and an efficient state observer is designed to estimate the capacitive current. The motor current output by the observer is used for the closed-loop control. Then, the capacitor current is obtained by subtracting the motor current from the inverter side current, and is used for resonance suppression. The block diagram of the proposed state observer is shown in Figure 9.
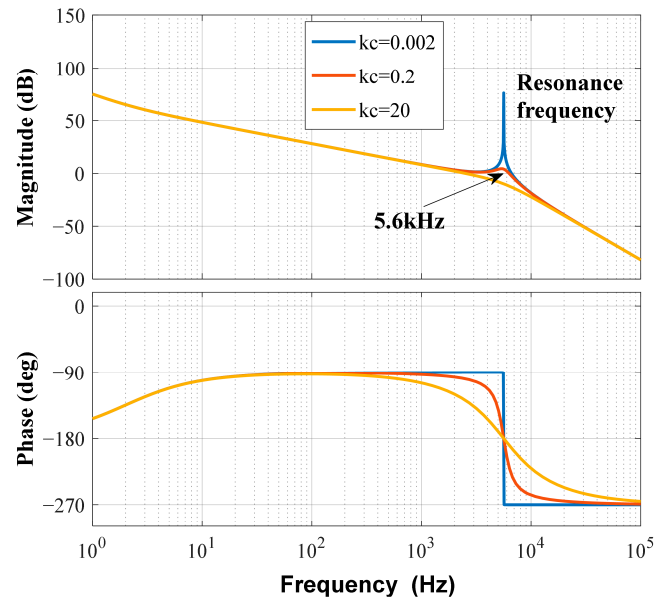
Figure 7. Bode diagram of the open-loop transfer function with the PI+CCFAD controller.
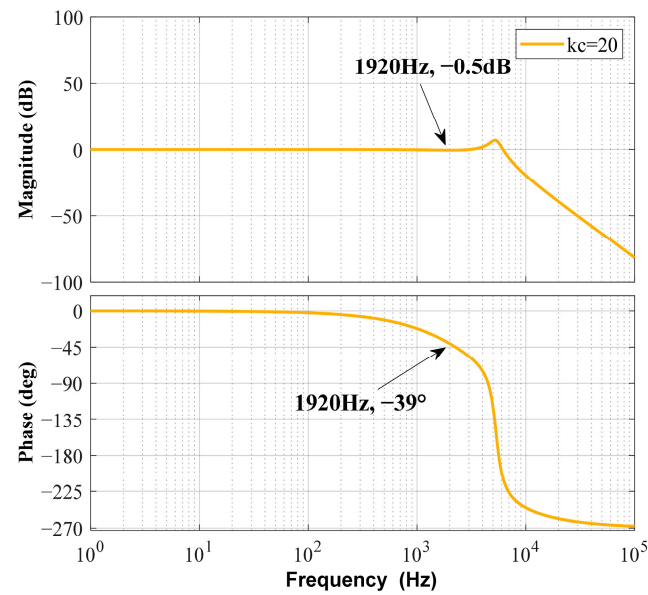

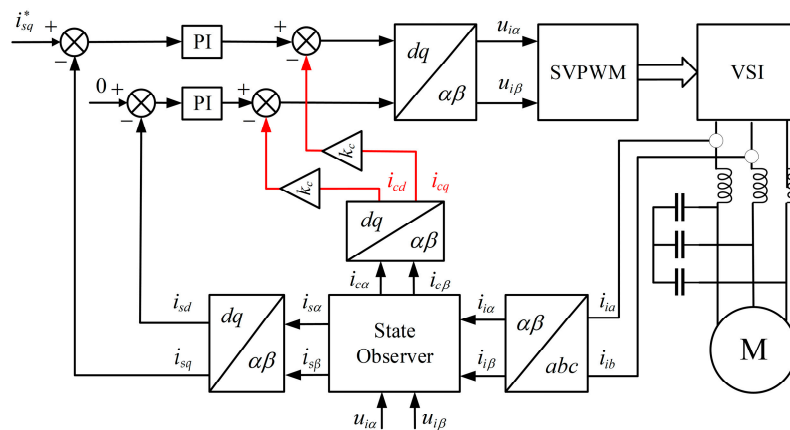**Figure 8.** Bode diagram of the closed-loop transfer function with the PI+CCFAD controller.

Figure 9. Current controller architecture with state observer CCFAD.

The LC filter and motor are regarded as a whole, and the system mathematical model can be rewritten as a state equation:

$$\begin{cases} \frac{di_{i\alpha}}{dt} = \frac{1}{L_f}u_{i\alpha} - \frac{1}{L_f}u_{s\alpha} \\ \frac{di_{i\beta}}{dt} = \frac{1}{L_f}u_{i\beta} - \frac{1}{L_f}u_{s\beta} \\ \frac{du_{s\alpha}}{dt} = \frac{1}{C_f}i_{i\alpha} - \frac{1}{C_f}i_{s\alpha} \\ \frac{du_{s\beta}}{dt} = \frac{1}{C_f}i_{i\beta} - \frac{1}{C_f}i_{s\beta} \\ \frac{di_{s\alpha}}{dt} = \frac{1}{L_s}u_{s\alpha} - \frac{R_s}{L_s}i_{s\alpha} - \frac{1}{L_s}e_{s\alpha} \\ \frac{di_{s\beta}}{dt} = \frac{1}{L_s}u_{s\beta} - \frac{R_s}{L_s}i_{s\beta} - \frac{1}{L_s}e_{s\beta} \end{cases} \tag{9}$$

The state space model can be described as follows:

$$\begin{cases} \frac{dx}{dt} = Ax + Bu \\ y = Cx \end{cases} \tag{10}$$

where A, B, and C are the system matrix; x is the state vector; u is the input vector; and y is the output vector.

The state vector of the control system is defined as

$$x = \left(i_{i\alpha}\ i_{i\beta}\ u_{s\alpha}\ u_{s\beta}\ i_{s\alpha}\ i_{s\beta} \right)^T \tag{11}$$

The input vector is defined as

$$u = \left(u_{i\alpha}\ u_{i\beta} \right)^T \tag{12}$$

The output vector is defined as

$$y = \left(i_{i\alpha}\ i_{i\beta} \right)^T \tag{13}$$

The system matrix is

$$A = \begin{bmatrix} 0 & 0 & -\frac{1}{L_f} & 0 & 0 & 0 \\ 0 & 0 & 0 & -\frac{1}{L_f} & 0 & 0 \\ \frac{1}{C_f} & 0 & 0 & 0 & -\frac{1}{C_f} & 0 \\ 0 & \frac{1}{C_f} & 0 & 0 & 0 & -\frac{1}{C_f} \\ 0 & 0 & \frac{1}{L_s} & 0 & -\frac{R_s}{L_s} & 0 \\ 0 & 0 & 0 & \frac{1}{L_s} & 0 & -\frac{R_s}{L_s} \end{bmatrix} \tag{14}$$

$$B = \begin{bmatrix} \frac{1}{L_f} & 0 & 0 & 0 & 0 & 0 \\ 0 & \frac{1}{L_f} & 0 & 0 & 0 & 0 \end{bmatrix}^T \tag{15}$$

$$C = \begin{bmatrix} 1 & 0 & 0 & 0 & 0 & 0 \\ 0 & 1 & 0 & 0 & 0 & 0 \end{bmatrix} \tag{16}$$

The sliding mode observer has the advantages of a fast response and strong robustness, and it is mathematically expressed as [26]

$$\frac{d\hat{x}}{dt} = A\hat{x} + Bu + L\text{sgn}(\hat{y} - y) \tag{17}$$

where $\hat{x}$ denotes the estimated state vector. The observer gain matrix L and sign function are denoted as

$$L = \begin{bmatrix} l_1 & 0 & l_2 & 0 & 0 & 0 \\ 0 & l_1 & 0 & l_2 & 0 & 0 \end{bmatrix}^T \tag{18}$$

where l_1 and l_2 are the sliding mode gains.

L is a constant matrix. It determines the dynamic performance of the observer. According to the pole configuration method, the observer pole should be located to the left of the subsystem pole. On this basis, the closer the observer pole is to the imaginary axis, the more robust it is, but the worse the transient response is; similarly, the farther the observer pole is from the imaginary axis, the faster the transient response is, and, at the same time, the worse the stability is. Therefore, the choice of L must be a trade-off. In general, the poles are chosen to be 4–6-times the poles of the system.

In order to reduce chattering, which is a drawback of the sliding mode observer, segmented power functions are chosen in this paper.

$$p(\zeta) = \begin{cases} 1 & \zeta \geq \sigma \\ \zeta^2/\sigma^2 & 0 \leq \zeta < \sigma \\ -\zeta^2/\sigma^2 & -\sigma < \zeta < 0 \\ -1 & \zeta \leq -\sigma \end{cases} \tag{19}$$

where ζ is the observed variable error and σ denotes a positive boundary layer.

The observation equation can be expressed as

$$\begin{cases} \frac{d\hat{i}_{i\alpha}}{dt} = \frac{1}{L_f}u_{i\alpha} - \frac{1}{L_f}\hat{u}_{s\alpha} + l_1(\hat{i}_{i\alpha} - i_{i\alpha}) \\ \frac{d\hat{i}_{i\beta}}{dt} = \frac{1}{L_f}u_{i\beta} - \frac{1}{L_f}\hat{u}_{s\beta} + l_1(\hat{i}_{i\beta} - i_{i\beta}) \\ \frac{d\hat{u}_{s\alpha}}{dt} = \frac{1}{C_f}i_{i\alpha} - \frac{1}{C_f}\hat{i}_{s\alpha} + l_2(\hat{u}_{s\alpha} - u_{s\alpha}) \\ \frac{du_{s\beta}}{dt} = \frac{1}{C_f}i_{i\beta} - \frac{1}{C_f}\hat{i}_{s\beta} + l_2(\hat{u}_{s\beta} - u_{s\beta}) \end{cases} \tag{20}$$

Then, the error state equation of the system can be concluded as (21) by subtracting (9) from (20)

$$\begin{cases} \frac{d(\hat{i}_{i\alpha} - i_{i\alpha})}{dt} = -\frac{1}{L_f}(\hat{u}_{s\alpha} - u_{s\alpha}) + l_1(\hat{i}_{i\alpha} - i_{i\alpha}) \\ \frac{d(\hat{i}_{i\beta} - i_{i\beta})}{dt} = -\frac{1}{L_f}(\hat{u}_{s\beta} - u_{s\beta}) + l_1(\hat{i}_{i\beta} - i_{i\beta}) \\ \frac{d(\hat{u}_{s\alpha} - u_{s\alpha})}{dt} = -\frac{1}{C_f}(\hat{i}_{s\alpha} - i_{s\alpha}) + l_2(\hat{u}_{s\alpha} - u_{s\alpha}) \\ \frac{d(\hat{u}_{s\beta} - u_{s\beta})}{dt} = -\frac{1}{C_f}(\hat{i}_{s\beta} - i_{s\beta}) + l_2(\hat{u}_{s\beta} - u_{s\beta}) \end{cases} \tag{21}$$

The design sliding mode control law is

$$\begin{cases} u_{s\alpha} = l_1 \, p(\hat{i}_{i\alpha} - i_{i\alpha}) \\ u_{s\beta} = l_1 \, p(\hat{i}_{i\beta} - i_{i\beta}) \end{cases} \tag{22}$$

$$\begin{cases} i_{s\alpha} = l_2 \, p(\hat{u}_{s\alpha} - u_{s\alpha}) \\ i_{s\beta} = l_2 \, p(\hat{u}_{s\beta} - u_{s\beta}) \end{cases} \tag{23}$$

From (22) and (23), the double sliding mode surfaces are designed to reduce the order of the system. When the state variable of the observer is stably tracking on the sliding surface, the dynamic behavior of the observer will continue to operate on the sliding surface according to the equivalent control theory of the sliding mode control. In this case, the control input applied to the system can be regarded as an equivalent control variable.

4. Harmonic Suppression with the PIR Controller

The coreless motor phase current also contains obvious fifth and seventh harmonics due to limited rotor optimization, and nonlinearity of the inverter. The PIR controller is

adopted to solve this problem. The closed-loop current control's structure after using the PIR controller is shown in Figure 10.

$$G_{\text{PIR}}(s) = K_p + \frac{K_i}{s} + \frac{2K_r \omega_c \, s}{s^2 + 2\omega_c \, s + \omega_0^2} \tag{24}$$
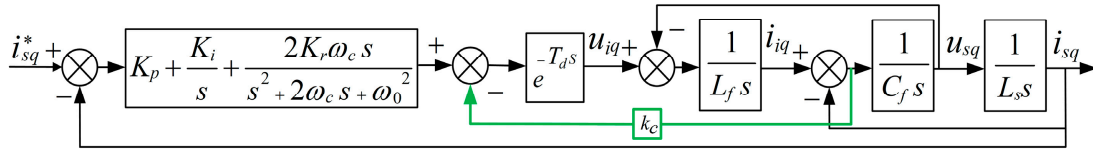

Figure 10. Block diagram of the PIR+CCFAD controller.

The transfer function of the PIR controller is expressed in (24). Where K_r is the PIR controller resonant gain, ω_c is the PIR controller resonant bandwidth, and ω_0 is the PIR controller resonant frequency. The corresponding open-loop transfer function of the system is derived as

$$G_{\text{PIR\_C}}(s) = \frac{K_p \, s^3 + (2K_p \, \omega_c + K_i + 2K_r \, \omega_c)s^2 + (K_p \, \omega_0^2 + 2K_i \, \omega_c)s + K_i \omega_0^2}{s(s^2 + 2\omega_c \, s + \omega_0^2)(L_f \, L_s \, C_f \, s^3 + k_c \, L_s \, C_f \, e^{-T_d S}s^2 + (L_f + L_s)s)} e^{-T_d S} \tag{25}$$

The proportional gain K_p determines the dynamic response of the system, which needs to be considered according to the current loop bandwidth; K_i is independent of harmonic suppression. When the motor speed fluctuation is large, an increase in the resonant bandwidth ω_c will help to enhance the current harmonic suppression effect, but too large an increase in the resonant bandwidth ω_c will lead to poor frequency selectivity. The resonance gain K_r is the most vital factor for the PIR controller to suppress harmonic currents. The larger K_r is, the better the suppression effect is, but too large a resonance gain in K_r will lead to system instability. In this paper, the control parameters are set to $K_p = 8$, $K_i = 100$, $K_r = 200$, $\omega_c = 15$, $L_f = 0.4$ mH, $C_f = 10$ μF, $L_s = 0.1$ mH, $T_d = 0.0000625$ s, and $k_c = 20$.

When the coreless motor is operating at 1600 rpm, the sixth harmonic current ω_0 in the dq-axis is 3840π rad/s and the PIR controller resonant frequency is 1920 Hz. The bode diagrams of the open-loop transfer function with the PIR controller are shown in Figure 11. It can be seen that the crossover frequency is 3270 Hz, and the corresponding phase margin is 55°. For the 1920 Hz input signal, the open-loop gain of the PIR controller is 32.5 dB, which is enough to eliminate the steady-state error. The bode diagrams of the closed-loop transfer function with the PIR controller are shown in Figure 12. It can be seen that the amplitude response at the PIR controller resonance frequency is −1.1 dB and the corresponding phase margin is −0.25°. The phase difference between the input signal and the output signal is close to 0°, so the PIR controller suppresses the harmonics current very well. Meanwhile, it can be seen that the active damping is still effective in suppressing the resonance peak at the resonance frequency of the LCL filter.
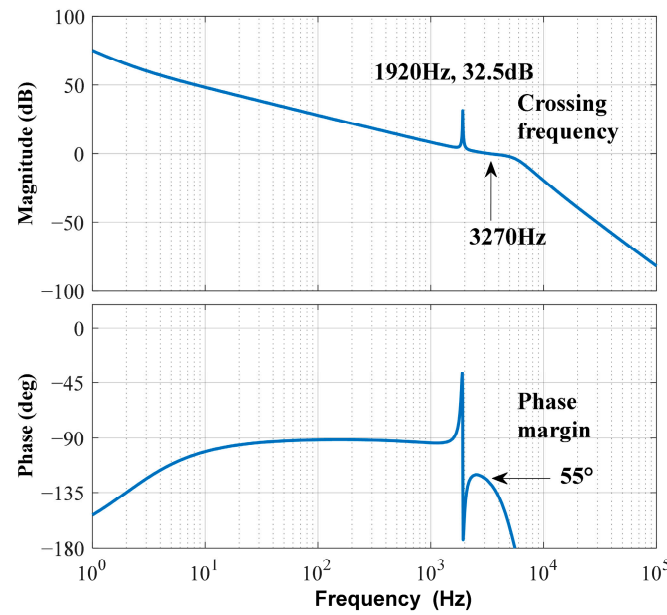
Figure 11. Bode diagram of the open-loop transfer function with the PIR+CCFAD controller.
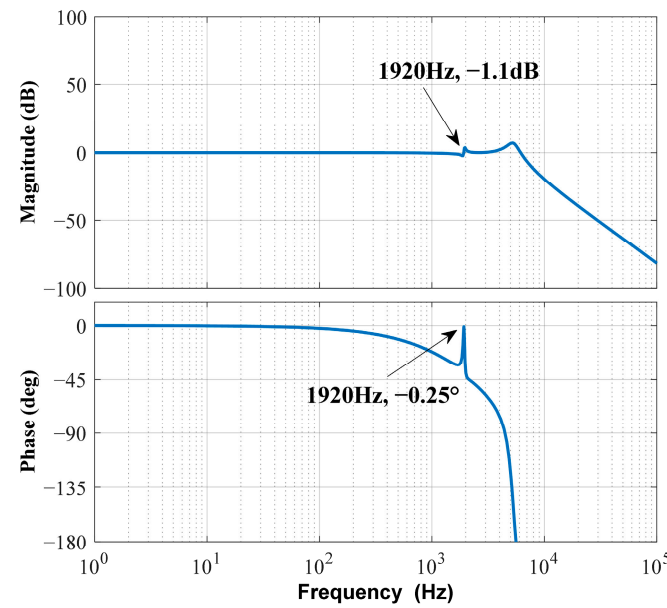

Figure 12. Bode diagram of the closed-loop transfer function with the PIR+CCFAD controller.

5. Experimental Verification

In order to verify the effectiveness of the control strategy based on the combination of proportional-integral-resonance and capacitor current damping proposed in this paper, a control platform is constructed, as shown in Figure 13. The coreless motor is driven by an insulated-gate bipolar transistor (IGBT) module. Harmonic current suppression strategies are implemented in the TMS320F28335D DSP. The switching frequency and sampling frequency are set to 16 kHz. The DC voltage is 311 V, and motor drive system parameters are listed in Table 1.

Table 1. Parameters of the coreless motor drive system.

Parameters	Value
Rated speed	3000 rpm
Rated torque	24 Nm
Stator inductance	0.1 mH

Table 1. *Cont.*

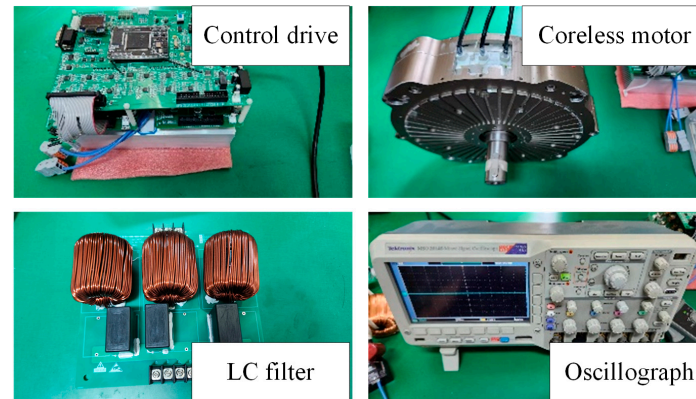| Parameters	Value
Stator resistance	0.3 Ω
Pole pairs	12
Rotor flux linkage	0.07873 Wb
Rated voltage	350 V
Rated current	13.5 A
L_f	0.4 mH
C_f	10 μF

Figure 13. Experimental platform for the coreless motor drive system.

5.1. Feasibility Experiment

Figures 14 and 15 shows the experimental waveforms and the FFT analysis results of phase currents corresponding to three control controllers when the speed is 800 rpm and the load torque is set to 12 Nm. As shown in Figure 14a, when active damping is not applied, the phase currents appear as an obvious oscillation phenomenon. According to the FFT analysis in Figure 15a, the THD is 18.68%. The maximum harmonic near the resonant frequency of the filter is 3.68% of the fundamental component, and the fifth and seventh harmonic currents are 7.86% and 2.14% of the fundamental component.
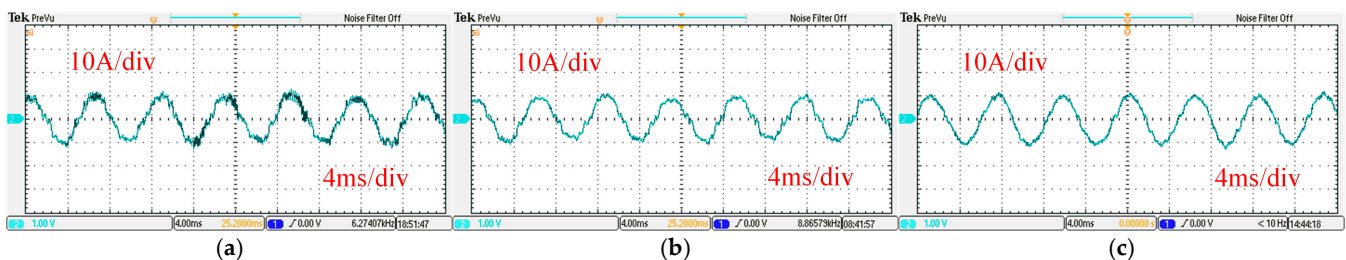

Figure 14. Experimental waveforms of the phase current under three different controllers with a speed of 800 rpm and a load torque of 12 Nm: (**a**) PI; (**b**) PI+CCFAD; (**c**) PIR+CCFAD.

As shown in Figure 14b, the phase current oscillation phenomenon disappears after the active damping is applied. According to the FFT analysis in Figure 15b, the THD is 14.68%. The maximum harmonic near the resonant frequency of the filter decreases from 3.68% to 1.08%, and the fifth and seventh harmonic currents are 7.96% and 2.61%. Obviously, using the active damping strategy can suppress resonance harmonics effectively.

As shown in Figure 14c, the current waveform is significantly improved due to the adoption of the PIR controller. According to the FFT analysis in Figure 15c, the THD is 10.96%. The maximum harmonic near the resonant frequency of the filter increases from 1.08% to 1.13%. The adoption of the PIR controller has no significant effect on the active damping. The fifth harmonic decreases from 7.96% to 1.3%, and the seventh harmonic

decreases from 2.61% to 0.88%. It can be seen that the fifth and seventh harmonics can be effectively suppressed by using the PIR controller.
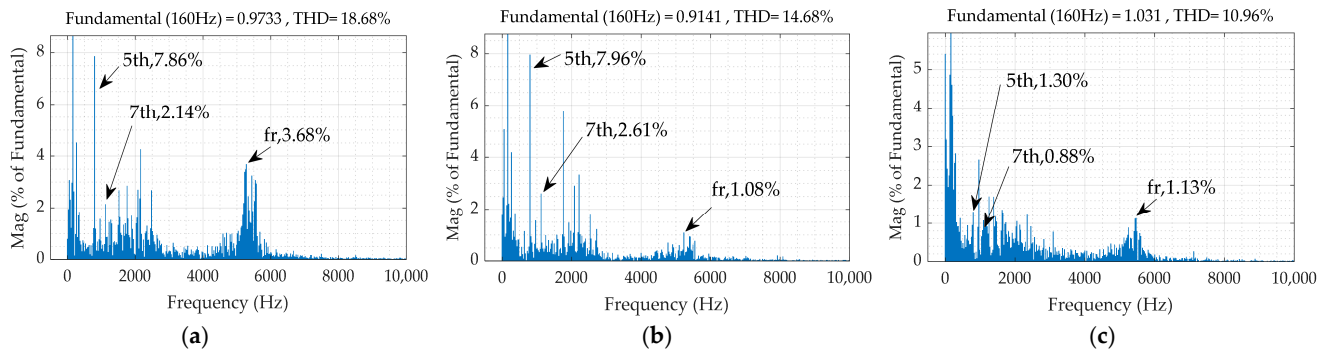

Figure 15. THD analysis of the phase current under three different controllers with a speed of 800 rpm and a load torque of 12 Nm: (**a**) PI; (**b**) PI+CCFAD; (**c**) PIR+CCFAD.

Similarly, Figures 16 and 17 show the experimental results when the speed is 1600 rpm. When the active damping strategy is not adopted, the THD is 27.13%. The maximum harmonic near the resonant frequency of the filter is 10.26%, and the fifth and seventh harmonic currents are 13.13% and 5.82%.
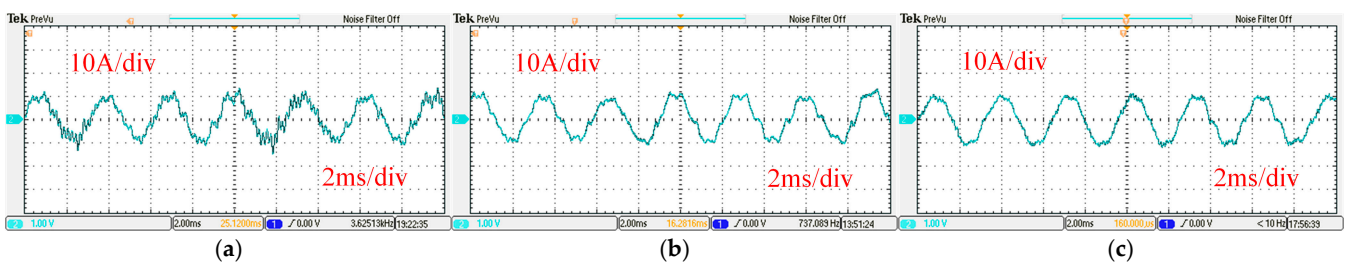

Figure 16. Experimental waveforms of the phase current under three different controllers with a speed of 1600 rpm and a load torque of 12 Nm: (**a**) PI; (**b**) PI+CCFAD; (**c**) PIR+CCFAD.
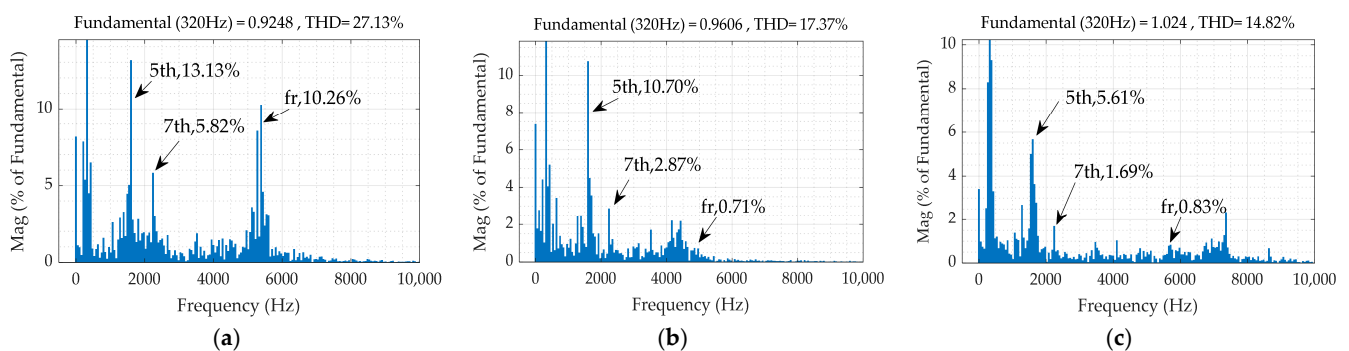

Figure 17. THD analysis of the phase current under three different controllers with a speed of 1600 rpm and a load torque of 12 Nm: (**a**) PI; (**b**) PI+CCFAD; (**c**) PIR+CCFAD.

When Figure 17a is compared with Figure 15a, the content of the fifth and seventh harmonics increased significantly, which is due to the decrease in the carrier ratio as the speed increases, resulting in a decrease in the control performance.

After the active damping strategy is adopted, the THD decreases from 27.13% to 17.37%. The maximum harmonic near the resonant frequency of the filter decreases from 10.26% to 0.71%. After the PIR controller is adopted, the THD decreases from 17.37% to 14.82%. The fifth harmonic decreases from 10.70% to 5.61%, and the seventh harmonic decreases from 2.87% to 1.69%. Therefore, the proposed control strategy can be adapted to a wide speed range.

Notably, after the PIR+CCFAD controller is adopted, the current THD decreases from 27.13% to 14.82%, which contributes to a significant reduction in power losses and an improved motor efficiency and stability. The results of the feasibility experiment are summarized in Table 2.

Table 2. Summary of feasibility experiments.

	Speed (rpm)	Torque (Nm)	THD (%)
PI	800	12	18.68
PI+CCFAD	800	12	14.68
PIR+CCFAD	800	12	10.96
PI	1600	12	27.13
PI+CCFAD	1600	12	17.37
PIR+CCFAD	1600	12	14.82

5.2. Performances Verified Under Different Filter Parameters

Figures 18 and 19 show the experimental results of the proposed PIR+CCFAD controller under different filter parameters. Figure 18a shows the experimental waveform after the filter capacitance is reduced from 10 μF to 4.7 μF. Comparing Figure 19a with Figure 15c, due to the reduction in filter capacitance, the cut-off frequency increases, and the current THD value increases from 10.96% to 11.27%, but it is still at a good level.
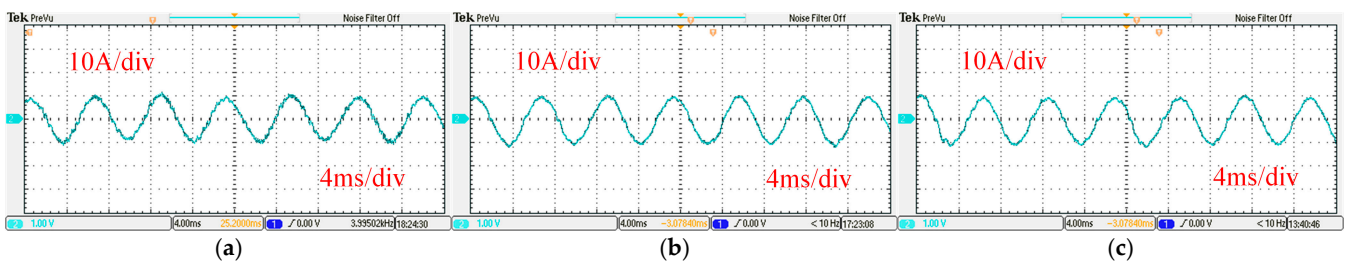

Figure 18. Experimental waveforms of the phase current under three different filter parameters with a speed of 800 rpm and a load torque of 12 Nm: (**a**) $L_f = 0.4$ mH, $C_f = 4.7$ μF; (**b**) $L_f = 0.8$ mH, $C_f = 4.7$ μF; (**c**) $L_f = 0.8$ mH, $C_f = 10$ μF.
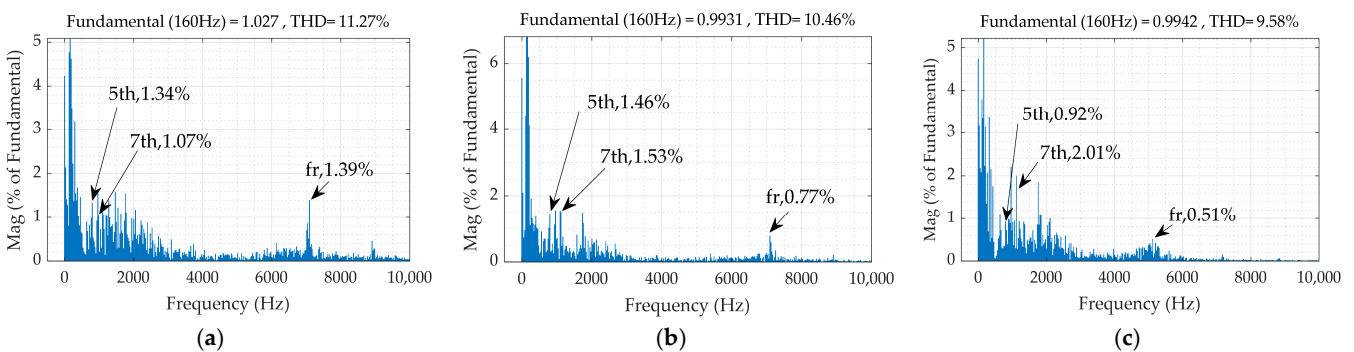

Figure 19. THD analysis of the phase current under three different filter parameters with a speed of 800 rpm and a load torque of 12 Nm: (**a**) $L_f = 0.4$ mH, $C_f = 4.7$ μF; (**b**) $L_f = 0.8$ mH, $C_f = 4.7$ μF; (**c**) $L_f = 0.8$ mH, $C_f = 10$ μF.

Figure 18b shows the experimental waveform with a filter inductance of 0.8mH and filter capacitance of 4.7 μF. Figure 18c shows the experimental waveform with a filter inductance of 0.8mH and filter capacitance of 10 μF. Compared with Figure 19a, the THD value of the current waveform in Figure 19b,c further decreases with the increase in filter inductance or filter capacitance. Therefore, the proposed control strategy can be adapted to

a wide range of LC filter parameters. The experimental results of different filter parameters are summarized in Table 3.

Table 3. Summary of different filter parameters' experiments.

L_f	C_f	Speed (rpm)	Torque (Nm)	THD (%)
0.4 mH	4.7 μF	800	12	11.27
0.4 mH	10 μF	800	12	10.96
0.8 mH	4.7 μF	800	12	10.46
0.8 mH	10 μF	800	12	9.58

6. Conclusions

In view of the resonance problem caused by the LC filter, an active damping control strategy based on a state observer is studied. Firstly, the causes of the resonance phenomenon are analyzed based on the mathematical model. The capacitive current feedback active damping is used to suppress the resonance phenomenon. In order to avoid adding additional current sensors, a new capacitive current feedback damping strategy is proposed, which estimates the capacitive current by introducing a state observer instead of the current sensor in the capacitive branch. The observer adopts the double sliding mode surface design, which effectively reduces the order of the system. In order to suppress the fifth and seventh harmonics at the same time, combined with the PIR controller, the overall performance of the coreless motor was further improved. The experimental results show that the designed PIR+CCFAD controller has a good control performance in the coreless motor control system. This will promote the application of the coreless motor in the field of transport, where the advantages of a small size and high efficiency are realized.

Author Contributions: Conceptualization, H.T.; methodology, H.T.; software, H.T. and M.K.; validation, H.T. and M.K.; formal analysis, H.T.; investigation, H.T.; resources, M.K.; data curation, H.T.; writing—original draft preparation, H.T.; writing—review and editing, H.T. and M.K.; visualization, H.T. and M.K.; supervision, M.K.; project administration, M.K.; funding acquisition, M.K. All authors have read and agreed to the published version of the manuscript.

Data Availability Statement: The data presented in this study are available in this article.

Conflicts of Interest: The authors declare no conflicts of interest.

References

1. Neethu, S.; Nikam, S.P.; Singh, S. High-Speed Coreless Axial-Flux Permanent-Magnet Motor with Printed Circuit Board Winding. *IEEE Trans. Ind. Appl.* **2019**, *55*, 1954–1962.
2. Zhang, Z.; Wang, C.; Geng, W. Design and Optimization of Halbach-Array PM Rotor for High-Speed Axial-Flux Permanent. Magnet Machine with Ironless Stator. *IEEE Trans. Ind. Electron.* **2020**, *67*, 7269–7279. [CrossRef]
3. Cheng, Z.; Li, L.; Pei, L.; Cao, J.; Liu, J. Analysis and Design of a Novel Dual-Trap LCL Inverter Output Filter for HS-PMSM Drives. *IEEE Access* **2024**, *12*, 109793–109805. [CrossRef]
4. Singh, S.K.; Pilli, N.K.; Guedon, F.; McMahon, R. PMSM drive using Silicon carbide Inverter: Development and Testing at Elevated temperature. In Proceedings of the IEEE International Conference on Industrial Technology, Seville, Spain, 17–19 March 2015.
5. Wang, K.; Zheng, Z.; Wei, D.; Fan, B. Topology and Capacitor Voltage Balancing Control of a Symmetrical Hybrid Nine-Level Inverter for High-Speed Motor Drives. *IEEE Trans. Ind. Appl.* **2017**, *53*, 5563–5572. [CrossRef]
6. Geng, W.; Zhang, Z.; Li, Q. Analysis and Experimental Verification of a Conventional Inverter with Output LC Filter to Drive Ironless Stator Axial-Flux PM Motor. *IEEE Trans. Tra. Electron.* **2021**, *7*, 2600–2610. [CrossRef]
7. Gao, Y.; Zhu, L.; Wang, K.; Lv, X.; Wei, H. A Novel Repeat PI Decoupling Control Strategy with Linear Active Disturbance Rejection for a Three-Level Neutral-Point-Clamped Active Power Filter with an LCL Filter. *Electronics* **2024**, *13*, 2973. [CrossRef]
8. Jayalath, S.; Hanif, M. An LCL-Filter Design with Optimum Total Inductance and Capacitance. *IEEE Trans. Power. Electron.* **2018**, *33*, 6687–6698. [CrossRef]

9.   Yao, Y.; Huang, Y.; Peng, F.; Dong, J.; Zhu, Z. Discrete-Time Dynamic-Decoupled Current Control for LCL-Equipped High-Speed Permanent Magnet Synchronous Machines. *IEEE Trans. Ind. Electron.* **2022**, *69*, 12414–12425. [CrossRef]

10.   Upadhyay, N.; Padhy, N.P.; Agarwal, P. Grid-Current Control with Inverter-Current Feedback Active Damping for LCL Grid-Connected Inverter. *IEEE Trans. Ind. Appl.* **2024**, *60*, 1738–1749. [CrossRef]

11.   Yao, W.; Yang, Y.; Zhang, B. Design and Analysis of Robust Active Damping for LCL Filters Using Digital Notch Filters. *IEEE Trans. Power. Electron.* **2017**, *32*, 2360–2375. [CrossRef]

12.   Liu, B.; Zhu, Y.; Guo, H. Analysis and design of passively damped LCL filters for three-phase converters. *Trans. China Electrotech. Soc.* **2017**, *32*, 195–205.

13.   Pena-Alzola, R.; Liserre, M.; Blaabjerg, F.; Sebastian, R.; Dannehl, J.; Fuchs, F.W. Analysis of the Passive Damping Losses in LCL-Filter-Based Grid Converters. *IEEE Trans. Power. Electron.* **2013**, *28*, 2642–2646. [CrossRef]

14.   Hatua, K.; Jain, A.K.; Banerjee, D.; Ranganathan, V. Active Damping of Output LC Filter Resonance for Vector-Controlled VSI-Fed AC Motor Drives. *IEEE Trans. Ind. Electron.* **2012**, *59*, 334–342. [CrossRef]

15.   Mishra, P.; Maheshwari, R.; Patil, D. Stabilization of Rotor Flux-Oriented Control of Induction Motor with Filter by Active Damping. *IEEE Trans. Ind. Electron.* **2019**, *66*, 9173–9183. [CrossRef]

16.   Mishra, P.; Maheshwari, R. A Simple Feedforward Approach to Stabilize VSI-Fed Induction Motor with Filter in RFOC. *IEEE Trans. Ind. Electron.* **2020**, *67*, 10191–10201. [CrossRef]

17.   Yang, M.; Lyu, Z.; Xu, D.; Long, J.; Shang, S.; Wang, P.; Xu, D. Resonance Suppression and EMI Reduction of GaN-Based Motor Drive with Sine Wave Filter. *IEEE Trans. Ind. Appl.* **2020**, *56*, 2741–2751. [CrossRef]

18.   Walz, S.; Liserre, M. Hysteresis model predictive current control for PMSM with LC filter considering different error shapes. *IEEE Open J. Power Electron.* **2020**, *1*, 190–197. [CrossRef]

19.   Xue, C.; Zhou, D.; Li, Y. Finite-Control-Set Model Predictive Control for Three-Level NPC Inverter-Fed PMSM Drives with LC Filter. *IEEE Trans. Ind. Electron.* **2021**, *68*, 11980–11991. [CrossRef]

20.   Liu, J.; Li, H.; Deng, H. Torque Ripple Minimization of PMSM Based on Robust ILC Via Adaptive Sliding Mode Control. *IEEE Trans. Power. Electron.* **2018**, *33*, 3655–3671. [CrossRef]

21.   Yu, J.; LI, L.; Du, P.; Zhang, J. Harmonic analysis of pivot current of high-speed permanent magnet synchronous motor. *Electr. Mach. Control* **2016**, *20*, 28–36.

22.   Li, Z.; Wu, H.; Chen, Z.; Shi, Y.; Qiu, L.; FANG, Y. Single- and Two-Phase Open-Circuit Fault Tolerant Control for Dual Three-Phase PM Motor Without Phase Shifting. *IEEE Access* **2020**, *8*, 171945–171955. [CrossRef]

23.   Yan, Y.; Lei, J.; Liu, B.; Xiang, X.; Li, C.; Li, W. Proportional Resonant Control with Phase Correction for Stability and Dynamics Enhancement Under Low Carrier Ratio Conditions. *IEEE Trans. Power. Electron.* **2023**, *38*, 8597–8611. [CrossRef]

24.   Cai, D.; Liu, H.; Hu, S.; Sun, G.; Wang, E. A Proportional-Integral-Resonant Current Control Strategy for a Wind-Driven Brushless Doubly Fed Generator during Network Unbalance. *Electronics* **2024**, *13*, 1616. [CrossRef]

25.   Wang, M.; Xu, Y.; Zou, J. Sliding mode control with open-switch fault diagnosis and sensorless estimation based on PI observer for PMSM drive connected with an LC filter. *IET Power Electron.* **2020**, *13*, 2334–2341. [CrossRef]

26.   Wu, X.; Li, C.; Zhang, Y.; Chen, S.; Ma, Z.; Han, Y. Sensorless Control of IPMSM Equipped with LC Sinusoidal Filter Based on Full-Order Sliding Mode Observer and Feedforward QPLL. *IEEE Trans. Power. Electron.* **2024**, *39*, 8072–8085. [CrossRef]